AGU PUBLICATIONS

JGR

Journal of Geophysical Research: Space Physics

RESEARCH ARTICLE
10.1002/2017JA024309

**Key Points:**
- Energetic electrons' response to geomagnetic activity vary with electron energy and L shell, viewed globally and locally
- Concurrent measurements by multiple satellites and balloons enable quantitative analysis of the precipitation of the energetic electrons
- A precipitation event is estimated to cause a loss of 6.8% of the total content for 0.58–1.63 MeV electrons in L = 3.5–6

**Correspondence to:**
K. Zhang,
kun.zhang@lasp.colorado.edu

**Citation:**
Zhang, K., X. Li, Q. Schiller, D. Gerhardt, H. Zhao, and R. Millan (2017), Detailed characteristics of radiation belt electrons revealed by CSSWE/REPTile measurements: Geomagnetic activity response and precipitation observation, *J. Geophys. Res. Space Physics*, *122*, 8434–8445, doi:10.1002/2017JA024309.

Received 27 APR 2017
Accepted 29 JUL 2017
Accepted article online 3 AUG 2017
Published online 19 AUG 2017



# Detailed characteristics of radiation belt electrons revealed by CSSWE/REPTile measurements: Geomagnetic activity response and precipitation observation

**K. Zhang[1,2], X. Li[1,2], Q. Schiller[3], D. Gerhardt[2], H. Zhao[1], and R. Millan[4]**

[1]Laboratory for Atmospheric and Space Physics, University of Colorado Boulder, Boulder, Colorado, USA, [2]Department of Aerospace Engineering Sciences, University of Colorado Boulder, Boulder, Colorado, USA, [3]Heliophysics Laboratory, NASA Goddard Space Flight Center, Greenbelt, Maryland, USA, [4]Department of Physics and Astronomy, Dartmouth College, Hanover, New Hampshire, USA

**Abstract** Earth's outer radiation belt electrons are highly dynamic. We study the detailed characteristics of relativistic electrons in the outer belt using measurements from the Colorado Student Space Weather Experiment (CSSWE) mission, a low Earth orbit (LEO) CubeSat, which traverses the radiation belt four times in one orbit (~1.5 h) and has the advantage of measuring the dynamic activities of the electrons including their rapid precipitation. We focus on the measured electron response to geomagnetic activity for different energies to show that there are abundant sub-MeV electrons in the inner belt and slot region. These electrons are further enhanced during active times, while there is a lack of >1.63 MeV electrons in these regions. We also show that the variation of measured electron flux at LEO is strongly dependent on the local magnetic field strength, which is far from a dipole approximation. Moreover, a specific precipitation band, which happened on 19 January 2013, is investigated based on the conjunctive measurement of CSSWE, the Balloon Array for Radiation belt Relativistic Electron Losses, and one of the Polar Operational Environmental Satellites. In this precipitation band event, the net loss of the 0.58–1.63 MeV electrons (L = 3.5–6) is estimated to account for 6.8% of the total electron content.

## 1. Introduction

Earth's radiation belt electrons constantly undergo different dynamic processes, including acceleration, transport, and loss. The fact that all these mechanisms interact with each other brings difficulties to the study of detailed processes and environmental modeling. Fortunately, a number of missions have been launched to observe these features. Especially during the Van Allen Probes operation period (2012–present), various in situ measurements from the heart of the radiation belt are available and widely used to explore the phenomena inside the radiation belt and the physics behind them [*Mauk et al.*, 2012]. Many discoveries and striking results have been obtained based on Van Allen Probes measurements [e.g., *Thorne et al.*, 2013; *Reeves et al.*, 2013; *Baker et al.*, 2013, 2014; *Zhao et al.*, 2014; *Foster et al.*, 2016; *Li et al.*, 2017].

On the other hand, satellites in geotransfer-like orbits, like the Van Allen Probes, which have an orbital period of ~9 h, miss some dynamic features of the radiation belt electrons. Additionally, at larger L, the loss cone near the equator is only a few degrees, so it is very difficult to determine the precipitation loss of the electrons by using such low-inclination satellites (L can be viewed as the geocentric distance in $R_E$ at the magnetic equator if the Earth's magnetic field is approximated as a dipole).

Satellites in geotransfer-like orbits are not ideal for measuring electrons in the inner belt because abundant energetic protons in the inner belt cause contamination to the electron measurements, which is hard to remove. For measuring inner belt electrons, low Earth orbit (LEO) measurements have an advantage. At low altitude, the measured inner belt protons are highly localized in the South Atlantic anomaly (SAA) region, which spans roughly from −90° to +40° in geographic longitude and −45° to 0° in geographic latitude. A large amount of electrons and protons can be measured in the SAA because the magnetic field strength there is relatively weak, and thus, particles have a lower mirror point and are more likely to reach the satellite altitude. Meanwhile, inner belt electrons can be measured in a larger region than that of the protons at the same altitude because of the faster pitch angle scattering rate of electrons [*Selesnick*, 2012]. Furthermore, the protons and electrons drift in opposite directions, which makes it possible for LEO satellites to detect inner belt electrons at the edge of the SAA influenced region.

Here we present a detailed description of radiation belt electron characteristics based on measurements from the Colorado Student Space Weather Experiment (CSSWE), which is in a highly inclined LEO orbit (480 km × 790 km, 65° inclination). CSSWE measures particles with small equatorial pitch angles but traverses the radiation belt four times in one orbit (~1.5 h), thus providing higher temporal resolution measurements in comparison with geotransfer-like orbit satellites such as the Van Allen Probes; increased temporal sampling allows investigation of the complex behavior of the radiation belt electrons from a different perspective. For example, we will show the global distribution of the measured radiation belt particles during both quiet and active geomagnetic times, as well as the distinguished orbital and nonorbital effects of LEO measurements. We also provide a quantified estimate of the precipitation loss of radiation belt electrons for a precipitation band event, when the concurrent balloon measurements and Polar Operational Environmental Satellites (POES) measurements are available.

An important balance to the processes that cause enhancements of radiation belt electron content is precipitation loss to the atmosphere. As illustrated in Figure 1, electrons in the bounce loss cone, which is determined by the local magnetic field strength for a given longitude (shown as the pink region), will precipitate within one bounce. Electrons in the drift loss cone will not precipitate until their mirror points reach 100 km (or lower) as they drift toward the SAA region, where the bounce loss cone opens up and these electrons are called quasi-trapped (shown as the blue region). Electrons with greater equatorial pitch angles are stably trapped in the radiation belt (shown as the green region) unless they are pitch angle scattered into the loss cone. It is evident from Figure 1 that the profiles of the drift loss cone versus the longitude can be different for different L shells under the International Geomagnetic Reference Field (IGRF) model [*Thébault et al.*, 2015], where the greatest drift loss cone is at about 0° (360°) longitude for L ~ 5 but at about 310° longitude for L ~ 1.5.

Rapid electron precipitation events are observed as sudden enhancement of flux by LEO missions [e.g., *Sandanger et al.*, 2007; *Tu et al.*, 2010; *Blum et al.*, 2013; *L. Blum et al.*, 2015a], because LEO satellites with high inclination are capable of measuring particles inside the loss cone. This kind of sudden enhancement in electron precipitations can last less than 1 s (microbursts) or as long as minutes (precipitation bands) [*Nakamura et al.*, 1995; *Blake et al.*, 1996; *O'Brien et al.*, 2004; *L. Blum et al.*, 2015a]. Many previous studies argue that the electron precipitation bands are closely related to the pitch angle scattering caused by electromagnetic ion cyclotron (EMIC) waves and typically happen in the dusk sector [e.g., *Summers et al.*, 1998; *L. Blum et al.*, 2015a; *L. W. Blum et al.*, 2015b]. EMIC waves are shown to be resonant with MeV electrons causing those electrons to precipitate both analytically and numerically [*Lyons and Thorne*, 1972; *Summers and Thorne*, 2003; *Ukhorskiy et al.*, 2010]. However, in cold and dense plasmas that predominantly occur at the dusk sector of the magnetosphere, i.e., in duskside plasmaspheric plumes, the minimum resonant energy can be lowered to less than 1 MeV at $L > 3$ [*Thorne and Kennel*, 1971; *Jordanova et al.*, 2008; *L. W. Blum et al.*, 2015b]. Another efficient way to scatter the relativistic electrons (for even lower energies) is via interaction with chorus waves, which can also cause microbursts [*Horne and Thorne*, 2003; *Thorne et al.*, 2005; *Kersten et al.*, 2011; *Artemyev et al.*, 2012; *L. Blum et al.*, 2015a]. Precipitation events have a significant influence on the radiation belt electron content. *Mourenas et al.* [2016] point out that the concurrent combination of intense whistler mode chorus waves and EMIC waves can produce electron dropout in very fast time scales of 2–10 h. *Millan et al.* [2002] identified nine precipitation events with an average duration of 40 min, reflecting the long-lasting feature of the precipitation events. *Blum et al.* [2013] estimate a certain precipitation band, which lasts for 1.5 h, to cause at least 5% of the total outer belt electron content.

Balloon missions in high-latitude regions are also able to measure electron precipitations. Since balloons drift slowly, they are able to stay in the precipitation regions for a longer time and thus can measure the electron precipitation for the entire duration of a precipitation event. In addition, it is common to have multiple balloons on duty at the same time. This kind of multipoint balloon mission enables the study of the spatial boundaries of individual precipitation events.

Multipoint observations combining different LEO satellites and/or balloons provide important information on the spatial and temporal extents of the electron precipitation events, enabling quantitative estimate of the precipitated electron loss from their concurrent measurements. However, only few studies have been carried out to quantify the electron precipitation loss in the radiation belt [e.g., *Millan et al.*, 2002; *Blum et al.*, 2013] and it is necessary to study more individual precipitation events to characterize typical electron net loss. In

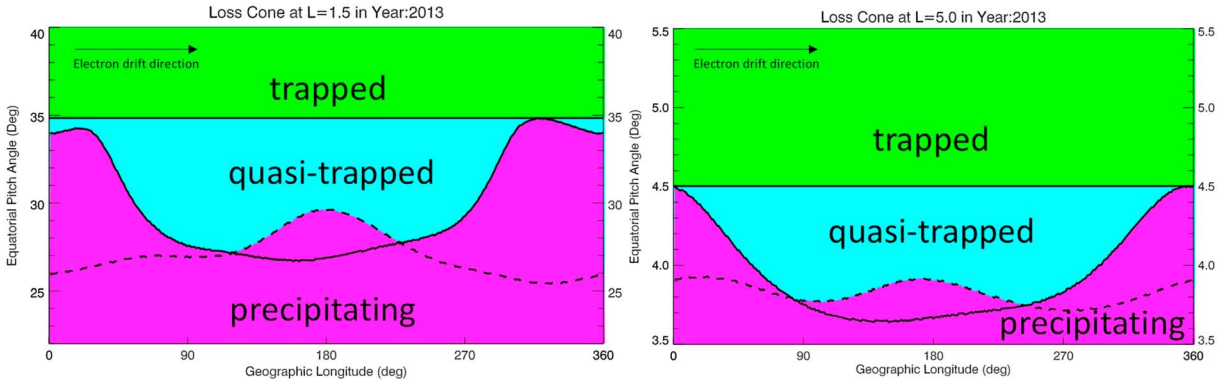


**Figure 1.** The loss cone calculated using the International Geomagnetic Reference Field (IGRF) model for different longitudes at (left) L ~ 1.5 and (right) L ~ 5. The solid curve is the largest equatorial pitch angle for the particles to precipitate in the southern hemisphere, and the dashed line is that for the particles to precipitate in the northern hemisphere. Particles in the green region are stably trapped, particles in the blue region are quasi-trapped (in the drift loss cone), and particles in the pink region are precipitating (in the bounce loss cone).

order to compare the net loss to the outer belt electron content, some previous studies on electron precipitations integrated the LEO measured flux over volume to get the estimate of the total electron content [e.g., *O'Brien et al.*, 2004; *Blum et al.*, 2013]. A more reliable way is to use electron distribution function measured near equatorial region and integrate it over velocity and volume [*Williams et al.*, 1976; *Zhao et al.*, 2015], which is applied in the quantitative estimation of electron precipitation for precipitation band event in this study.

## 2. Observation and Discussion

### 2.1. Instrument Description

CSSWE is a LEO CubeSat designed, built, and operated by students at University of Colorado Boulder with close mentorship from professionals and was deployed into orbit on 13 September 2012 with an inclination of 65° and 480 km × 790 km altitude [*Li et al.*, 2012, 2013]. The sole science instrument onboard CSSWE is the Relativistic Electron and Proton Telescope integrated little experiment (REPTile), which measures the electron and proton flux with a time resolution of 6 s. REPTile uses the energy deposit (threshold) of each particle to determine the species and uses the penetration depth to determine the energy of the particle [*Schiller and Mahendrakumar*, 2010; *Blum and Schiller*, 2012; *Li et al.*, 2012; *Schiller et al.*, 2014]. REPTile has three energy channels for both electrons and protons: 0.58–1.63 MeV, 1.63–3.8 MeV, and >3.8 MeV for electrons (referred to as the first, second, and third channels hereinafter) and 9–18 MeV, 18–30 MeV, and 30–40 MeV for protons. REPTile has a field of view of 52° with the pointing direction wobbling around the perpendicular direction to the background magnetic field (Figure 2). Since the electron distribution typically peaks at the local pitch angle of 90°, REPTile observes the vast majority of the local electrons throughout the orbit. Due to the asymmetric geomagnetic field structure, REPTile may measure trapped particles that are dominant, quasi-trapped particles that are in the drift loss cone, and also precipitating particles in the bounce loss cone, depending on the location of the measurement.

Measurements from the 2013 Balloon Array for Radiation belt Relativistic Electron Losses (BARREL) campaign and POES are also used to complement our analysis of electron precipitation. BARREL is a set of balloons carrying X-ray spectrometers designed to measure the bremsstrahlung X-rays produced by precipitating relativistic electrons [*Millan et al.*, 2013; *Woodger et al.*, 2015]. Note that since BARREL does not measure electrons directly, the count rate that BARREL measures at a certain energy channel does not scale straightly to the electron flux with that energy. In fact, it is common that BARREL observed precipitations in low-energy channels are more significant than that in higher-energy channels which the relativistic electron precipitation is supposed to happen in, e.g., *Blum et al*. [2013] and *Woodger et al*. [2015]. During the precipitation event studied in this paper, there were five balloons distributed in different locations at 27–37 km above Antarctica. These multiple-point measurements provide valuable information on the temporal and spatial ranges of the precipitation event. Meanwhile, the Medium Energy Proton and Electron Detector onboard POES 19 also observed this event in its >612 keV electron channel, which was originally designed to measure >6174 keV

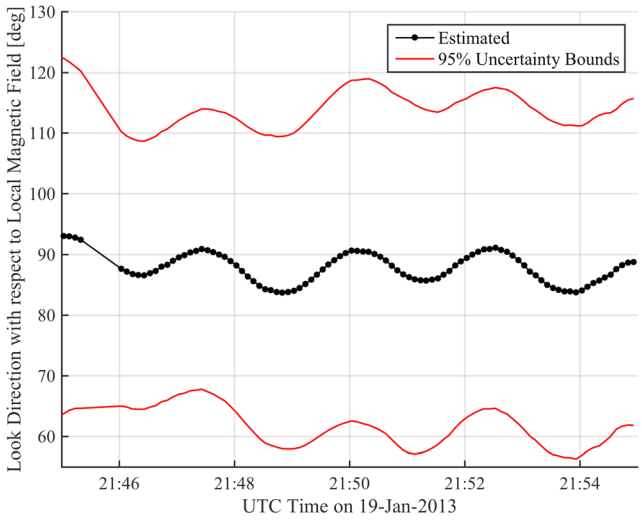


**Figure 2.** The estimated look direction of REPTile with respect to the local geomagnetic field, represented by the black line, on 19 January 2013 when a precipitation event was measured by REPTile, which will be discussed later in the paper. The red lines indicate the 95% uncertainty bounds.

protons but is also sensitive to >612 keV electrons, and is approximately the same energy range as REPTile's first channel for electrons [*Yando et al.*, 2011]. POES 19 is in a low-altitude polar orbit with an inclination of 98.74° and an altitude of 854 km.

### 2.2. Global Distribution of Energetic Particles Measured by REPTile

At the altitude of CSSWE, the local geomagnetic features such as SAA are significant. The fluxes measured by REPTile are highly dependent on its latitude and longitude. We plot the particle flux measured by REPTile over a Mercator map to better present the features of the radiation belts. In Figure 3, we present a 10 day quiet time period from 4 to 14 January 2013, during which the minimum *Dst* index only reached −30 nT and also a 20 day active time period from 1 to 20 July 2013 when three medium geomagnetic storms happened in a row and the minimum *Dst* reached −98 nT. The inner belt, slot region (which is usually considered to be in the L shell range of 1.8–2.8 for MeV electrons as shown between the blue traces in both hemispheres), and outer belt can be seen in these figures. We only show the proton measurements during the active time period because the inner belt protons are relatively stable and do not show any discernable variation with geomagnetic activities. We also note that there are no solar proton events during either time period.

Figure 3 provides a global picture of the energetic particle distribution. High electron and proton fluxes are measured around the SAA region, forming the large red region on the plot. However, the spatial extent of this region is very different between the first electron channel and the proton channels, which indicates that there are indeed low-energy electrons in the inner belt, in addition to the contamination from energetic protons at the center of SAA. Furthermore, the electron flux in the SAA and slot region is higher during the active period, which shows that electron injections are more likely to happen in active times and that ~600 keV electrons can penetrate through the slot region. In contrast, the morphology of the second and third channel electrons around the SAA region resembles the morphology of the protons. The >1.63 MeV electrons tend to be less influenced by geomagnetic activity, and no penetration through the slot region can be seen in these moderate storms. It is also evident from comparing the outer belt electron fluxes between these two period that the first channel electron (0.58–1.63 MeV) fluxes are much enhanced during the active period, with higher-energy channels showing less obvious enhancements.

The electrons' variations described above are consistent with other recent studies based on the Van Allen Probes MagEIS measurements. *Turner et al.* [2015] examined the electron response to 52 storms and found that <600 keV electrons are typically seen enhanced in up to 87% of the storms at L ~ 3.7, while >~1 MeV electrons result in no enhancement in most events at L < 4 and produce enhancement in only about 40% of the events at L > 4. They also showed that the locations of the peak flux move earthward in about 70% of the cases for 590 keV electrons and about 50% of the cases for 1050 keV electrons, with one specific

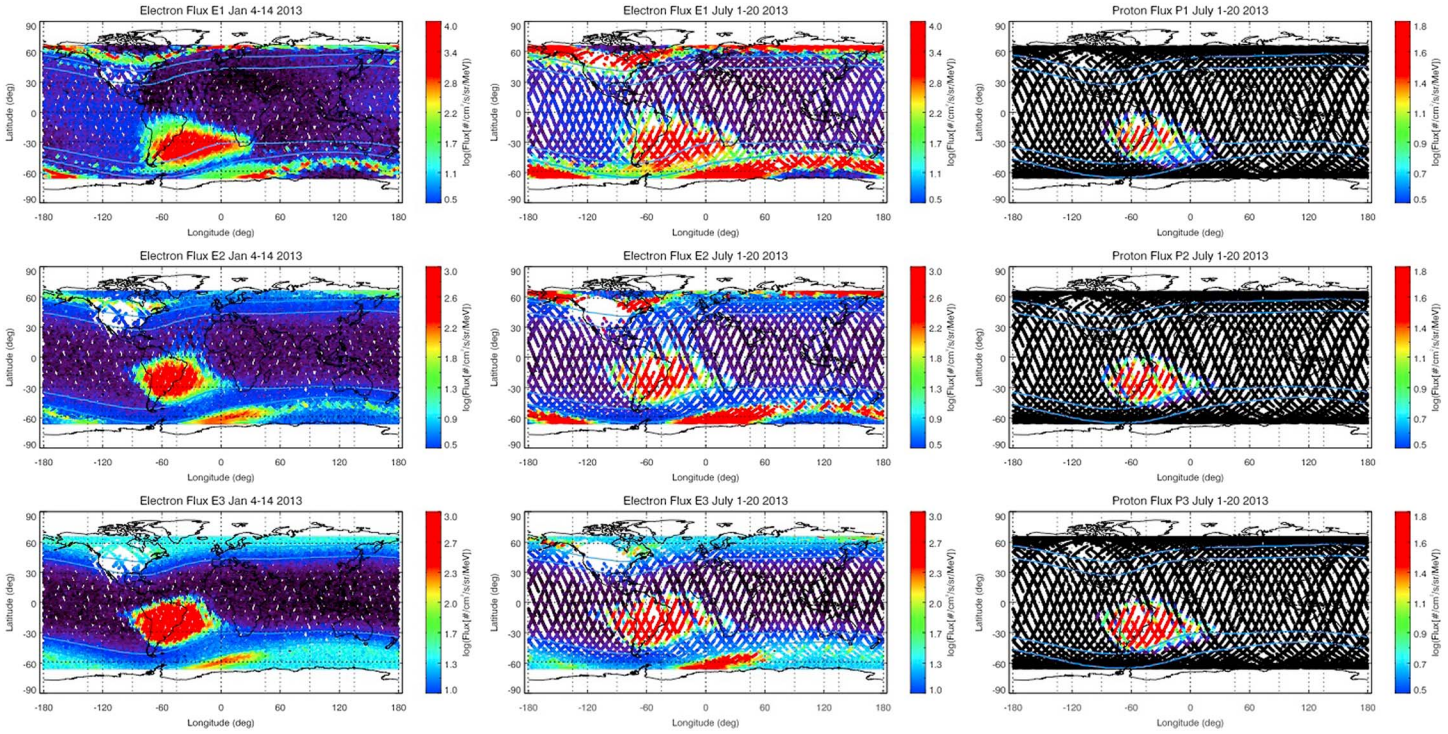


**Figure 3.** REPTile measured particle fluxes, color-coded, plotted with Mercator maps. The blue lines show the location of L = 1.8 and 2.8, and the region between is considered as the slot region. (left column) Electron fluxes in the quiet time window from 4 to 14 January 2013. (middle) Electron flux in the active time window from 1 to 20 July 2013. (right) Proton flux in the same active period as the middle column. In each column, from top to bottom are the energy channel 1 (0.58–1.63 MeV for electrons or 9–18 MeV for protons), channel 2 (1.63–3.8 MeV for electrons or 18–30 MeV for protons), and channel 3 (>3.8 MeV for electrons or 30–40 MeV for protons). The duty cycle of REPTile was lower in July of 2013, leading to more data gaps.

case showing that the 590 keV electrons penetrate 0.5 $R_E$ deeper than the 1050 keV electrons in L shell. *Reeves et al*. [2016] showed in the whole year of 2013 that no event extended below L ~ 3 for 1.5 MeV electrons, while at least seven events penetrate through the slot region for 459 keV electrons. They concluded that in any given event, lower energy electrons are more likely to penetrate through the slot regions into the inner belt, which was also demonstrated and discussed by *Zhao et al*. [2016].

More detailed features of the electrons are revealed in Figure 4, in which we plot the measured electron fluxes for the first and second channels against geographic longitude in a quiet time period for the inner belt, slot region, and outer belt in the top, middle, and bottom rows respectively. Also plotted is the corresponding IGRF magnetic field strength. The variation of the electron flux versus the longitude for each panel is shown to be highly consistent with the local geomagnetic field strength, where a valley in the magnetic field strength profile is accompanied with a peak in the electron flux at that location but a drop in the electron flux in the conjugated region in the other hemisphere. This feature is clearest in Figure 4 (top left), the first channel in the inner belt ($1.45 < L < 1.55$), which indicates that electrons are more affected by the SAA and North Pacific Anomaly (NPA), marked as yellow and blue regions, respectively, in Figure 4 (top left), for lower energy and in lower L. Moreover, due to the relatively weaker geomagnetic field near the SAA and NPA regions, electrons in the drift loss cone (shown as blue color region in Figure 1) precipitate into the atmosphere when they drift into the precipitating region (marked in pink in Figure 1) near the SAA or NPA, which is most evident at SAA corresponding to the flux drop at longitude 280° for northern measurements. As the electrons drift eastward, a gradual refill of the drift loss cone is expected due to pitch angle scattering [e.g., *Selesnick*, 2012]. This can be seen as the positive slope in electron flux between longitude 40° and 270° in Figure 4 (top left), which strongly suggests that these are indeed electrons, not inner belt protons, which would drift westward [*Li et al.*, 2015]. The positive slope can be seen in the inner belt, slot region, and outer belt in the first channel, which indicates that electrons in this energy range exist in all of the three regions. However, for the second channel electrons, this feature is only observed in the outer belt, indicating that there are no measured >1.63 MeV electrons above the background noise level outside of the SAA region in either the inner belt or slot

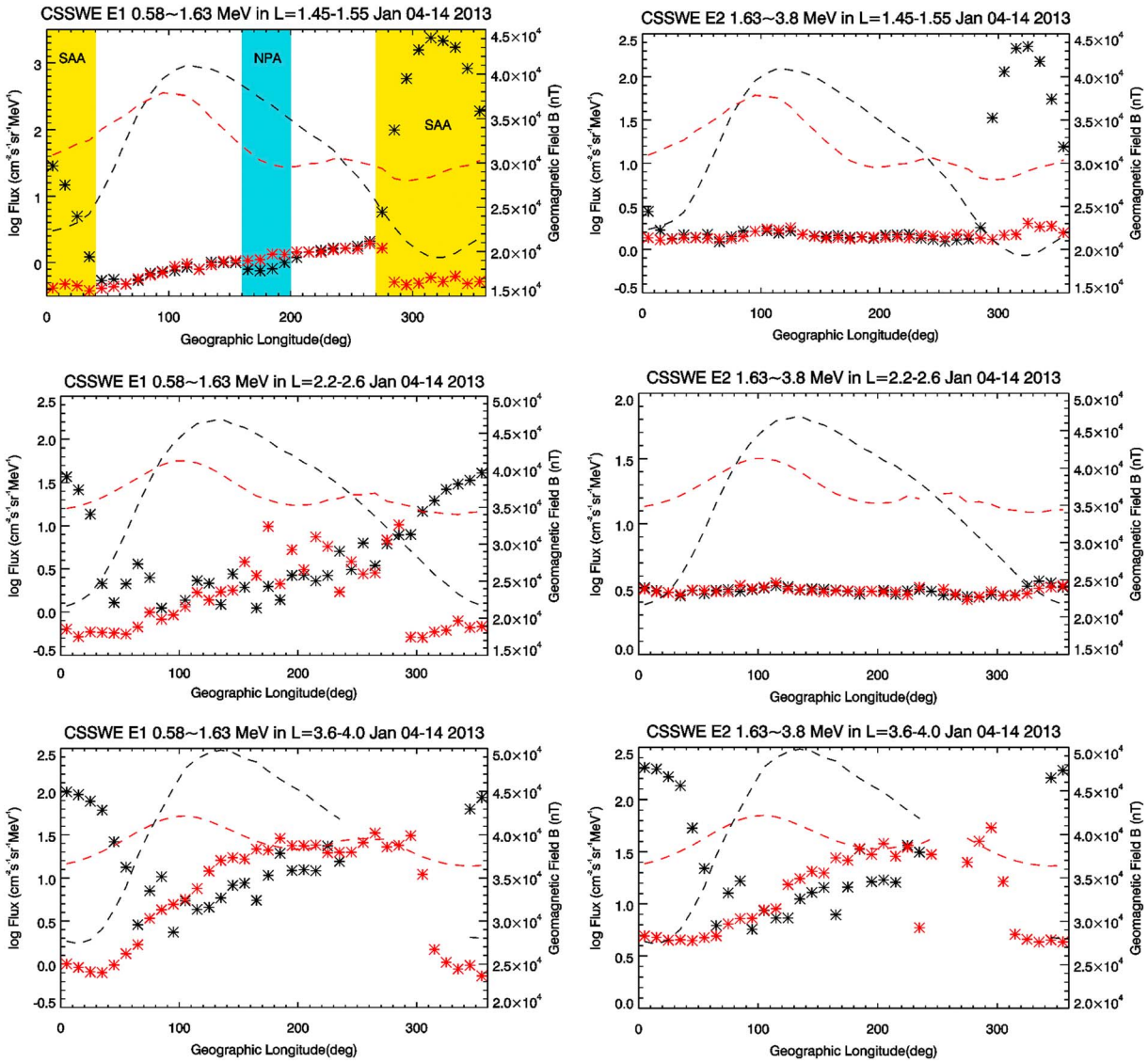


**Figure 4.** Averaged electron flux versus longitude as measured by REPTile (stars). The averaged geomagnetic field strength under IGRF model is plotted as dashed lines. Measurements in the southern hemisphere are black and in the northern are red. The flux measurements are filtered by L shell range for the (top row) inner belt, (middle row) slot region, and (bottom row) outer belt. (left column) The first channel fluxes and (right column) the second channel fluxes. The approximate longitude ranges for the SAA and North Pacific Anomaly (NPA) are marked yellow and blue, respectively, in the top left plot.

region. Note that the second electron channel has higher background noise than the first channel. However, the positive slope feature is evident for >1.63 MeV electrons in the outer belt (Figure 4, bottom right), which suggests that it is harder for high-energy electrons to penetrate and stay in the slot region and the inner belt.

### 2.3. Orbital and Nonorbital Effect of LEO Measurement

A LEO satellite samples particles with different (equatorial) pitch angles at different times as the spacecraft experiences different local magnetic fields; thus, both orbital and nonorbital effects contribute to the changes in the measured fluxes. In Figure 5, we show electron flux profiles of two consecutive orbits of CSSWE on 10 and 19 January 2013, such that (1b) is 1.5 h later than (1a) and (2b) is 1.5 h later than (2a). On 10 January, the early pass (1a) shows a high flux in $L < 2.5$ for both channels, while the following pass (1b) shows a moderate flux increase in the first channel at a similar L. The change in flux is due to the orbital effect of LEO measurement: in the second pass, CSSWE does not go into the SAA region where a clear inner belt pattern can be seen, while it went through the heart of the SAA region in the first pass, measuring a higher inner belt electron flux in a lower magnetic field strength environment (where more electrons have

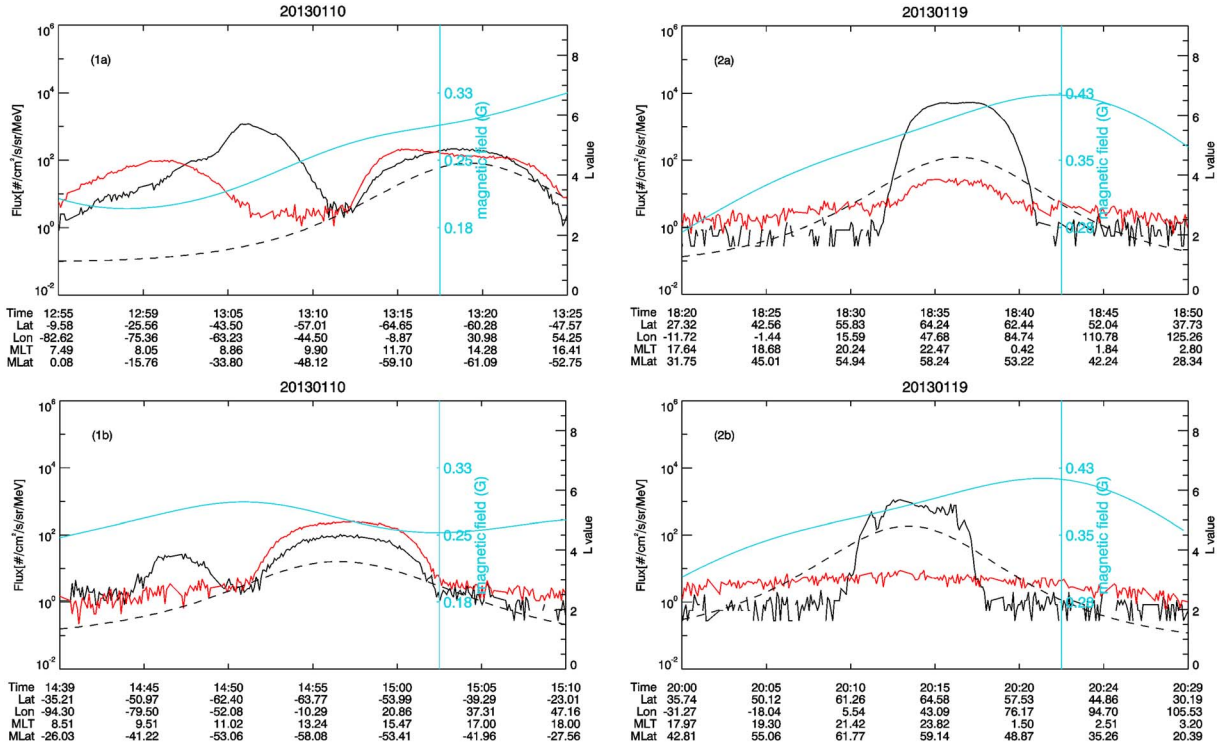


**Figure 5.** REPTile measured electron flux profile. The black solid line indicates the 0.58–1.63 MeV electron flux; the red line indicates the 1.63–3.8 MeV electron flux; the dashed line indicates the L value; the blue line indicates the magnetic field strength. (1a) and (1b) are consecutive orbits passing the same hemisphere and show an orbital effect on the measurement. (2a) and (2b) are consecutive orbits showing the internal dynamic changes of the radiation belt.

their mirror points at or below the satellite altitude), even though the longitude is only about 10° apart for the two consecutive passes. In contrast, the difference of the measured fluxes between the two consecutive passes on 19 January is not due to orbital effects: the flux profile in the early pass (2a) is smooth, but in the later pass (2b) it is disturbed and decreased, even though the background magnetic field is comparable. Indeed, it shows that REPTile measures a real dynamic change of the radiation belt that happened within 1.5 h, and the disturbance in the later pass eventually grew into a rapid electron precipitation event that is discussed in the next section. The magnetic field strength profiles look similar for the two passes on 19 January, while the early pass on 10 January clearly went into a region with weaker magnetic field than the later pass and sampled the inner belt. The weakness of the magnetic field strength in the early pass led to higher electron fluxes measured by REPTile. Therefore, even though LEO satellites are capable of observing radiation belt change in a short time scale, orbital effects have to be carefully considered in the procedure.

### 2.4. The 19 January 2013 Precipitation Band

On 19 January 2013, REPTile observed an electron precipitation band in the energy range of 0.58–3.8 MeV at about 21:47 and L ~ 4.5 (Figure 6b). Because CSSWE orbits rapidly, REPTile is only able to measure a spike in the electron flux and quickly moved out of the precipitation region. The BARREL 1C X-ray detector also observed an enhancement that extended to >500 keV, starting almost at the same time and lasting for about 15 min (Figure 6a), during which its 605 keV channel observed a much higher count rate than the average level of the day. The precipitation event indicated by BARREL 1C measurements and the precipitation band measured by REPTile are considered as the same event based on the simultaneity. In addition, a further enhancement of the BARREL 1C X-ray measurement at about 21:53 happened concurrently with a small spike measured by REPTile, which again suggests that those two measurements are related to each other.

The conjunctive measurements between spacecraft and balloons allow to estimate the extent of the region over which the precipitation happened in. In this case, the spatial extent of measured precipitation is L ~ (4.48, 4.81) and magnetic local time (MLT) ~ (20.6, 21.4) by REPTile as well as L ~ (6.89, 6.56) and

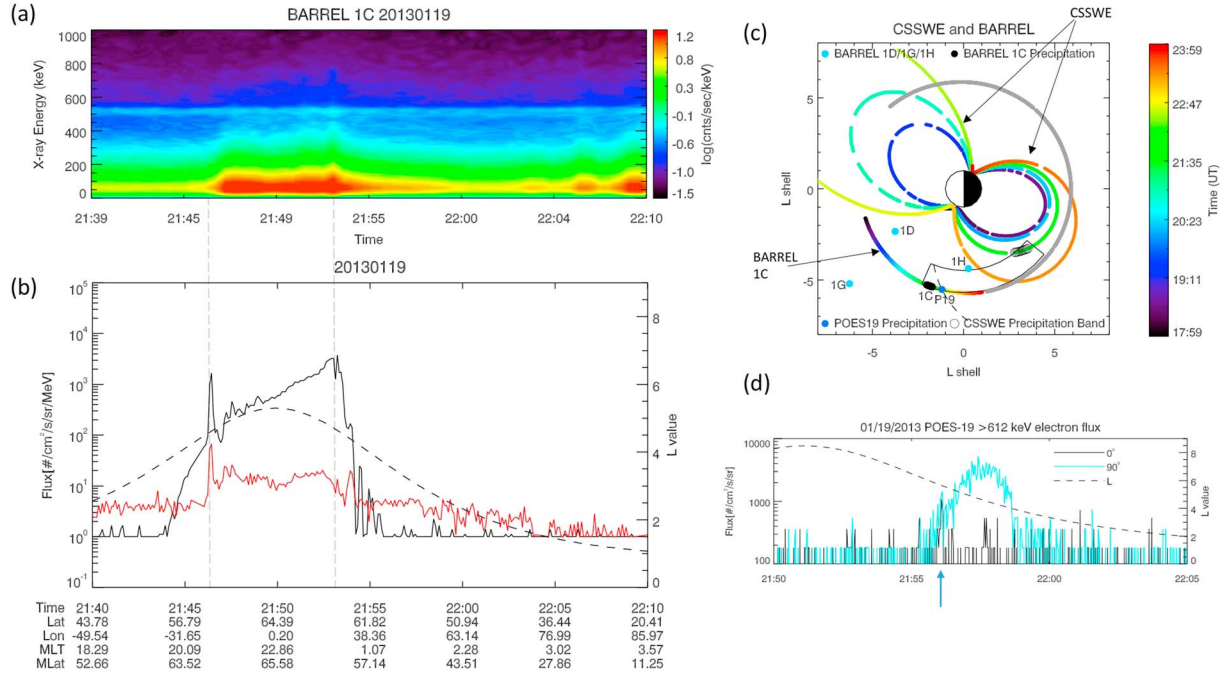


**Figure 6.** Multipoint measurement of the 19 January 2013 precipitation event and the locations of the measurements. (a) X-ray spectrum of the 19 January 2013 precipitation event measured by BARREL 1C (32 sec resolution). (b) REPTile electron flux measurement with the precipitation band between the two gray vertical lines. The black solid line indicates the 0.58–1.63 MeV electron flux; the red line indicates the 1.63–3.8 MeV electron flux; the dashed line indicates the L value. (c) The location of CSSWE, BARREL 1C, and POES 19 measurements of the electron precipitation event mapped to the equatorial plane using the IGRF model. Radial distance represents the L shell and the polar angle indicates MLT with noon to the left. The color of the trajectory shows the universal time of the location, with gray indicating that the measurement is beyond the time range shown in the color bar. The estimated precipitation region is determined by the CSSWE and BARREL 1C location and bounded by the black solid lines. A small portion of POES 19 trajectory is shown as the dashed line, and its measurement of the precipitation band falls in the estimated precipitation region. Other balloons on duty which did not observe precipitation are shown as light blue dots. (d) POES 19 measurement of the precipitation event with a precipitation band seen at 21:56 (marked by the blue arrow).

MLT ~ (16.4, 16.8) by BARREL. Therefore, we determine the precipitation region to be within the L shell range of (4.48, 6.89) and the MLT range of (16.4, 21.4) (all calculated under the IGRF model). In order to validate the estimate, we checked other available measurements. In total, there were five balloons of the BARREL campaign on duty during the precipitation event including 1C and no others observed any precipitation. Excluding the one that is too far away from the precipitation region, the other three balloons, namely, 1D, 1G, and 1H are shown as blue dots and are assumed to be located out of the precipitation region. In addition, one of the POES, POES 19, measured precipitating electrons in its 0° detector (parallel to the local magnetic field line) during this time period and based on the morphology study of POES precipitation bursts by *Yahnin et al.* [2014], a precipitation band is identified at about 21:57 (Figure 6d). Figure 6c presents the locations of CSSWE, BARREL balloons, and the POES 19 satellite mapped to the equator using the IGRF field model and the estimated precipitation region. By mapping the location of the POES 19 measured precipitation band to the geomagnetic equatorial plane, it is found that this precipitation band was close to the BARREL 1C's location and also fell in the precipitation region determined by the conjunctive measurement of CSSWE and BARREL 1C. Therefore, while not used to constrain the precipitation region, the POES measurement supports that REPTile and BARREL 1C observed the same precipitation event, though it cannot fully confirm this statement. Furthermore, *L. W. Blum et al.* [2015b] showed that on 19 January 2013 at around 22:00, EMIC waves were observed by GOES 13 concurrently with the BARREL 1C measured precipitation event, indicating that this precipitation event is possibly driven by the interaction between EMIC waves and the relativistic electrons.

### 2.5. Estimate of the Electron Net Loss Due To a Precipitation Band

The area of the precipitation region at CSSWE altitude is estimated to be $1.72 \times 10^6$ km$^2$ by assuming the precipitation region to be a surface element ($dS = r^2 \sin\theta d\theta\, d\phi$) in spherical coordinates, where $r = R_E + h$ is the radial distance; $h$ is the altitude of CSSWE (789.4 km during the event); $\theta = 90° - \lambda$, where $\lambda$ is the

geomagnetic latitude; and $\phi$ represents geomagnetic longitude. Thus, we write the area of the precipitation region as

$$\boldsymbol{A} = \Delta(\sin\lambda)\cdot\Delta\boldsymbol{\phi}\cdot(\boldsymbol{R_E}+\boldsymbol{h})^2 \tag{1}$$

Together with the precipitated electron flux measured by REPTile and the duration given by BARREL 1C, we can calculate the total net loss of the electrons using the method described by *O'Brien et al*. [2004] and *Blum et al*. [2013]. To augment these studies, we refine their measurements by taking the loss cone into consideration here. The local loss cone near the precipitation region is about 60° (assuming that the particles that reach 100 km altitude are lost and calculated with IGRF model). Since the POES measurements indicate that the electrons in the precipitation region have isotropic pitch angle distribution based on the comparable flux levels measured by the 0° and 90° detectors, the simplified equation of the number of precipitated electrons is

$$\#\boldsymbol{e} = 2\Delta\boldsymbol{f}\cdot\Delta\boldsymbol{T}\cdot\boldsymbol{A}\cdot\boldsymbol{\Omega} \tag{2}$$

where $\Delta f$ is the peak flux of the precipitation band above the background flux with the trapped flux covered under the background flux, $\Delta T$ is the duration of the event, and $\Omega$ is the solid angle converted from the local loss cone. Because the precipitation event is measured in both north (CCSWE) and south (BARREL) hemispheres, the total net loss is doubled, assuming that the electrons are lost equally in amount in both hemispheres. In the 19 January 2013 event, we take $\Delta f = 1608.46\ \mathrm{cm^{-2}s^{-1}sr^{-1}MeV^{-1}}$ for the first electron channel and $\Delta f = 56.54\ \mathrm{cm^{-2}s^{-1}sr^{-1}MeV^{-1}}$ for the second channel. Also, we take $\Delta T = 15$ min from the observation of BARREL 1C, assuming that the precipitation occurs continuously during this period and over the entire precipitation region. As for the result, we calculate the total net loss of this precipitation event to be $1.45\times10^{23}$ for the first electron channel and $5.08\times10^{21}$ for the second channel.

To get a better idea of the significance of the precipitated electrons, we use the electron flux measured by the Magnetic Electron Ion Spectrometer (MagEIS) onboard Van Allen Probe A to calculate the total electron content of the outer radiation belt. Based on the method adopted by *Williams et al*. [1976] and *Zhao et al*. [2015], we get the total electron content by integrating the distribution function. First, we calculate the number density of the electrons ($n$) by integrating the distribution function over velocity:

$$\boldsymbol{n} = \int \boldsymbol{f}\, \boldsymbol{dv}^3 = 2\pi\int_{\boldsymbol{v_1}}^{\boldsymbol{v_2}} \boldsymbol{v}^2\boldsymbol{dv}\int_0^{\pi}\boldsymbol{f}(\alpha)\sin\boldsymbol{\alpha}\boldsymbol{d\alpha} \tag{3}$$

where $\boldsymbol{f}$ is the distribution function and $f = \frac{dN}{dv^3dx^3}$, $\boldsymbol{N}$ is the number of electrons, $\boldsymbol{v}$ is the velocity, $\boldsymbol{\alpha}$ is the pitch angle, and $\boldsymbol{v}_1$ and $\boldsymbol{v}_2$ are the lower and upper velocity limits of the targeted particle population**.** Under the assumption of the magnetic momentum conservation, we write the number density as

$$\frac{\boldsymbol{n} = 4\pi\int_{\boldsymbol{v_1}}^{\boldsymbol{v_2}}\boldsymbol{v}^2\boldsymbol{dv}\int_0^{\alpha_m}\boldsymbol{f}(\alpha_0)\cdot\frac{\boldsymbol{B}}{\boldsymbol{B_0}}\cdot\sin\alpha_0\cos\alpha_0}{\sqrt{1-\frac{\boldsymbol{B}}{\boldsymbol{B_0}}(\sin\alpha_0)^2}\boldsymbol{d\alpha_0}} \tag{4}$$

where $\boldsymbol{B}$ is the magnetic field strength. The subscript 0 represents equatorial value and $\boldsymbol{\alpha_m} = \boldsymbol{\sin}^{-1}\left(\sqrt{\frac{\boldsymbol{B_0}}{\boldsymbol{B}}}\right)$. Under the dipole assumption, $\frac{\boldsymbol{B}}{\boldsymbol{B_0}} = \frac{\sqrt{1+3\boldsymbol{sin}^2\lambda}}{\boldsymbol{cos}^6\lambda}$. Then we integrate the number density over a flux tube. The volume of the flux tube is

$$\boldsymbol{V_{FT}} = \int\boldsymbol{A}_0\cdot\frac{\boldsymbol{B}_0}{\boldsymbol{B}}\boldsymbol{dl} = 2\int_0^{\lambda_m}\boldsymbol{A}_0\boldsymbol{r}_0\boldsymbol{cos}^7\lambda\boldsymbol{d\lambda} \tag{5}$$

where $\boldsymbol{A}_0$ is the cross-section area of the flux tube; $\boldsymbol{r}_0$ is the distance from the flux tube to the center of the Earth, both at equator; and $\boldsymbol{l}$ is the length of the magnetic field line. Here $\boldsymbol{dl} = \boldsymbol{r}_0\cos\lambda\sqrt{1+3sin^2\lambda}$ and $\boldsymbol{\lambda_m}$ is the maximum geomagnetic latitude that the flux tube reaches. We can substitute $\boldsymbol{\lambda_m}$ with the geomagnetic latitude of the mirror point, $\lambda_{mir}$, using the relation $\int_0^{\lambda_m}\int_0^{\alpha_m}d\alpha_0 d\lambda = \int_0^{\frac{\pi}{2}}\int_0^{\lambda_{mir}(\alpha_0)}d\lambda d\alpha_0$. The approximate value of integral $\int_0^{\lambda_{mir}(\alpha_0)}\frac{\cos\lambda\left(1+3sin^2\lambda\right)^{\frac{1}{2}}}{\sqrt{1-\frac{\left(1+3sin^2\lambda\right)^{\frac{1}{2}}}{cos^6\lambda}sin^2\alpha_0}}d\lambda \approx 1.30-0.56\sin\alpha_0$ [*Roederer*, 1970] is taken. Then we get the total electron content in a flux tube assuming that the electron density is uniform in the flux tube:

$$N_{FT} = 8\pi A_0 r_0 \int_{v_1}^{v_2} v^2 dv \int_0^{\frac{\pi}{2}} f(\alpha_0) \sin\alpha_0 \cos\alpha_0 (1.30 - 0.56 \sin\alpha_0) d\alpha_0 \quad (6)$$

We assume that in a flux tube of the dipole field, $f(\alpha_0) = \frac{m}{v^2} j(\alpha_0)$ , $j(\alpha_0) = j_0 \sin^{\gamma}\alpha_0$, and $\gamma = 2.5$ [from *Gannon et al.*, 2007], where $j(\alpha_0)$ is the measured flux of particles with equatorial pitch angle of $\alpha_0$ and $j_0$ is the flux of particles with 90° pitch angle at magnetic equator. Note that under this assumed pitch angle distribution, the electron fluxes measured by REPTile are quantatively comparable to the corresponding MagEIS channel after mapping the LEO fluxes to the equatorial regions (not shown here). We thus convert the measured spin-averaged flux into $j_0$. Converting the velocity integral into the energy, the total electron content in a flux tube is calculated as

$$N_{FT} = 8\pi A_0 r_0 \int_{E1}^{E2} \sqrt{\frac{m}{2E}} \left( \frac{1.3}{\gamma + 2} - \frac{0.56}{\gamma + 3} \right) j_0 dE \quad (7)$$

where $E1$ and $E2$ are the corresponding energy limits of the particles in velocity range $[v_1, v_2]$. The energy range we choose here is from 583 to 1697 keV, in order to match the REPTile first electron channel measurement. Lastly, we add up the electron content for all the flux tubes in 0.1 L bins and get the total electron content.

The calculation result shows that there are $2.24 \times 10^{24}$ electrons in an L range of 3 to 6.5 based on the averaged flux on 19 January 2013 by MagEIS. The total net loss of this precipitation event has been shown to be $1.45 \times 10^{23}$ electrons, corresponding to the net loss of 6.5% of the total electron content in the outer radiation belt. And there are $2.12 \times 10^{24}$ electrons in L = 4.5–6.5 where the precipitation event happened, corresponding to the net loss of 6.8% of the total electron content in this L shell range. Note that this time period was rather quiet, so the slot region expanded beyond L = 4. Therefore, the result for the two different L range are very similar.

## 3. Summary and Conclusions

Based on the measurements from CSSWE, an LEO CubeSat that has a short orbital period well suited to observe temporal features of radiation belt dynamics, as well as a high inclination to measure the trapped, quasi-trapped, and precipitating particles, we provide a broad and detailed description of radiation belt electron observations in the LEO environment and also discuss their various dynamic features. A multipoint observed precipitation event on 19 January 2013 is analyzed using measurements from CSSWE, BARREL, and POES missions. The resulting net loss of electrons associated with this event is estimated. In summary, this study reaches the following conclusions:

1. When comparing observations during geomagnetically active and quiet times, the averaged electron flux tends to be higher and the slot region is filled with ~600 keV electrons in the active period. However, the energetic proton flux is relatively stable and not affected by geomagnetic activity significantly. Also, the slot region is more difficult to access for higher-energy (>1.63 MeV) electrons, even during active times, than for lower energy (~600 keV) electrons.
2. Conjunctive measurements of CSSWE, BARREL, and POES are used to investigate an electron precipitation event. Combining the multipoint measurements helps constrain the spatial and temporal boundaries of the events.
3. For the 19 January 2013 21:50 precipitation band event, combining information collected from low Earth orbit environment and geotransfer orbit, 6.8% of the total electron content in L = 3.5–6 is estimated to be lost for the energy range of 0.58–1.63 MeV.

**Acknowledgments**
All CSSWE, BARREL, POES, and Van Allen Probes data used in this study are publicly available at http://cdaweb.gsfc.nasa.gov. The authors thank the BARREL team, Allison Jaynes, Samuel Califf, and Chen Shi for valuable discussion and additional help. This work was supported in part by NSF CubeSat/magnetospheric program grant AGS 1443749 and NASA grant NNX15AF56G, a subcontract (FA9453-14-M-0256) from the Air Force Research Laboratory, and by NASA/RBSP-ECT funding through JHU/APL contract 967399 under prime NASA contract NAS5-01072.

## References

Artemyev, A. V., V. V. Krasnoselskikh, O. V. Agapitov, D. Mourenas, and G. Rolland (2012), Non-diffusive resonant acceleration of electrons in the radiation belts, *Phys. Plasmas*, *19*, 122901, doi:10.1063/1.4769726.

Baker, D. N., et al. (2013), A long-lived relativistic electron storage ring embedded within the Earth's outer Van Allen Radiation Zone, *Science*, *340*(6129), 186–190, doi:10.1126/science.1233518.

Baker, D. N., et al. (2014), An impenetrable barrier to ultrarelativistic electrons in the Van Allen radiation belts, *Nature*, *515*, 7528, doi:10.1038/nature13956.

Blake, J. B., M. D. Looper, D. N. Baker, R. Nakamura, B. Klecker, and D. Hovestadt (1996), New high temporal and spatial resolution measurements by SAMPEX of the precipitation of relativistic electrons, *Adv. Space Res.*, *18*, 171–186.

Blum, L. W., and Q. G. Schiller (2012), Characterization and testing of an energetic particle telescope for a CubeSat platform, Small Satellite Conference, AIAA/USU.

Blum, L. W., Q. Schiller, X. Li, R. Millan, A. Halford, and L. Woodger (2013), New conjunctive CubeSat and balloon measurements to quantify rapid energetic electron precipitation, *Geophys. Res. Lett.*, *40*, 5833–5837, doi:10.1002/2013GL058546.

Blum, L., X. Li, and M. Denton (2015a), Rapid MeV electron precipitation as observed by SAMPEX/HILT during high-speed stream-driven storms, *J. Geophys. Res. Space Physics*, *120*, 3783–3794, doi:10.1002/2014JA020633.

Blum, L. W., et al. (2015b), Observations of coincident EMIC wave activity and duskside energetic electron precipitation on 18–19 January 2013, *Geophys. Res. Lett.*, *42*, 5727–5735, doi:10.1002/2015GL065245.

Foster, J. C., P. J. Erickson, D. N. Baker, A. N. Jaynes, E. V. Mishin, J. F. Fennel, X. Li, M. G. Henderson, and S. G. Kanekal (2016), Observations of the impenetrable barrier, the plasmapause, and the VLF bubble during the 17 March 2015 storm, *J. Geophys. Res. Space Physics*, *121*, 5537–5548, doi:10.1002/2016JA022509.

Gannon, J. L., X. Li, and D. Heynderickx (2007), Pitch angle distribution analysis of radiation belt electrons based on Combined Release and Radiation Effects Satellite Medium Electrons A data, *J. Geophys. Res.*, *112*, A05212, doi:10.1029/2005JA011565.

Horne, R. B., and R. M. Thorne (2003), Relativistic electron acceleration and precipitation during resonant interactions with whistler-mode chorus, *Geophys. Res. Lett.*, *30*(10), 1527, doi:10.1029/2003GL016973.

Jordanova, V. K., J. Albert, and Y. Miyoshi (2008), Relativistic electron precipitation by EMIC waves from self-consistent global simulations, *J. Geophys. Res.*, *113*, A00A10, doi:10.1029/2008JA013239.

Kersten, K., C. A. Cattell, A. Breneman, K. Goetz, P. J. Kellogg, J. R. Wygant, L. B. Wilson III, J. B. Blake, M. D. Looper, and I. Roth (2011), Observation of relativistic electron microbursts in conjunction with intense radiation belt whistler-mode waves, *Geophys. Res. Lett.*, *38*, L08107, doi:10.1029/2011GL046810.

Li, X., et al. (2012), Colorado Student Space Weather Experiment: Differential flux measurements of energetic particles in a highly inclined low Earth orbit, in *Dynamics of the Earth's Radiation Belts and Inner Magnetosphere*, *Geophys. Monogr. Ser.*, vol. 199, edited by D. Summers et al., pp. 385–404, AGU, Washington, D. C., doi:10.1029/2012GM001313.

Li, X., et al. (2013), First results from CSSWE CubeSat: Characteristics of relativistic electrons in the near-Earth environment during the October 2012 magnetic storms, *J. Geophys. Res. Space Physics*, *118*, 6489–6499, doi:10.1002/2013JA019342.

Li, X., R. S. Selesnick, D. N. Baker, A. N. Jaynes, S. G. Kanekal, Q. Schiller, L. Blum, J. Fennell, and J. B. Blake (2015), Upper limit on the inner radiation belt MeV electron intensity, *J. Geophys. Res. Space Physics*, *120*, 1215–1228, doi:10.1002/2014JA020777.

Li, X., D. N. Baker, H. Zhao, K. Zhang, A. N. Jaynes, Q. Schiller, S. G. Kanekal, J. B. Blake, and M. Temerin (2017), Radiation belt electron dynamics at low L ($<4$): Van Allen Probes era versus previous two solar cycles, *Blood Transfus.*, *122*, doi:10.1002/2017JA023924.

Lyons, L. R., and R. M. Thorne (1972), Parasitic pitch angle diffusion of radiation belt particles by ion cyclotron waves, *J. Geophys. Res.*, *77*, 5608–5616, doi:10.1029/JA077i028p05608.

Mauk, B. H., N. J. Fox, S. G. Kanekal, R. L. Kessel, D. G. Sibeck, and A. Ukhorskiy (2012), Science objectives and rationale for the radiation belt storm probes mission, *Space Sci. Rev.*, *179*, 1–15, doi:10.1007/s11214-012-9908-y.

Millan, R. M., R. P. Lin, D. M. Smith, K. R. Lorentzen, and M. P. McCarthy (2002), X-ray observations of MeV electron precipitation with a balloon-borne germanium spectrometer, *Geophys. Res. Lett.*, *29*(24), 2194, doi:10.1029/2002GL015922.

Millan, R. M., et al. (2013), The Balloon Array for RBSP Relativistic Electron Losses (BARREL), *Space Sci. Rev.*, *179*, 503–530, doi:10.1007/s11214-013-9971-z.

Mourenas, D., A. V. Artemyev, Q. Ma, O. V. Agapitov, and W. Li (2016), Fast dropouts of multi-MeV electrons due to combined effects of EMIC and whistler mode waves, *Geophys. Res. Lett.*, *43*, 4155–4163, doi:10.1002/2016GL068921.

Nakamura, R., D. N. Baker, J. B. Blake, S. Kanekal, B. Klecker, and D. Hovestadt (1995), Relativistic electron precipitation enhancements near the outer edge of the radiation belt, *Geophys. Res. Lett.*, *22*, 1129–1132, doi:10.1029/95GL00378.

O'Brien, T. P., M. D. Looper, and J. B. Blake (2004), Quantification of relativistic electron microburst losses during the GEM storms, *Geophys. Res. Lett.*, *31*, L04802, doi:10.1029/2003GL018621.

Reeves, G., et al. (2013), Electron acceleration in the heart of the Van Allen radiation belts, *Science*, *341*, 991–994, doi:10.1126/science.1237743.

Reeves, G. D., et al. (2016), Energy- dependent dynamics of keV to MeV electrons in the inner zone, outer zone, and slot regions, *J. Geophys. Res. Space Physics*, *121*, 397–412, doi:10.1002/2015JA021569.

Roederer, J. G. (1970), *Dynamics of Geomagnetically Trapped Radiation*, Springer, New York.

Sandanger, M., F. Søraas, K. Aarsnes, K. Oksavik, and D. S. Evans (2007), Loss of relativistic electrons: Evidence for pitch angle scattering by electromagnetic ion cyclotron waves excited by unstable ring current protons, *J. Geophys. Res.*, *112*, A12213, doi:10.1029/2006JA012138.

Schiller, Q., and A. Mahendrakumar (2010), REPTile: A miniaturized detector for a CubeSat mission to measure relativistic particles in near-Earth space, paper SSC10-VIII-1 presented at 24th Annual AIAA/USU Conference on Small Satellites, Frank J. Redd Student Scholarship Competition, Logan, Utah, 9–12 Aug.

Schiller, Q., D. Gerhardt, L. Blum, X. Li, S. Palo (2014), Design and scientific return of a miniaturized particle telescope onboard the Colorado Student Space Weather Experiment (CSSWE) CubeSat, 35th IEEE Aerospace Conference, 8.1102, doi:10.1109/AERO.2014.6836372.

Selesnick, R. S. (2012), Atmospheric scattering and decay of inner radiation belt electrons, *J. Geophys. Res.*, *117*, A08218, doi:10.1029/2012JA017793.

Summers, D., and R. M. Thorne (2003), Relativistic electron pitch-angle scattering by electromagnetic ion cyclotron waves during geomagnetic storms, *J. Geophys. Res.*, *108*(A4), 1143, doi:10.1029/2002JA009489.

Summers, D., R. M. Thorne, and F. Xiao (1998), Relativistic theory of wave-particle resonant diffusion with application to electron acceleration in the magnetosphere, *J. Geophys. Res.*, *103*(A9), 20,487–20,500, doi:10.1029/98JA01740.

Thébault, E., et al. (2015), International Geomagnetic Reference Field: The 12th generation, *Earth Planets Space*, *67*(1), 1–19, doi:10.1186/s40623-015-0228-9.

Thorne, R. M., and C. F. Kennel (1971), Relativistic electron precipitation during magnetic storm main phase, *J. Geophys. Res.*, *76*(19), 4446–4453, doi:10.1029/JA076i019p04446.

Thorne, R. M., T. P. O'Brien, Y. Y. Shprits, D. Summers, and R. B. Horne (2005), Timescale for MeV electron microburst loss during geomagnetic storms, *J. Geophys. Res.*, *110*, A09202, doi:10.1029/2004JA010882.

Thorne, R. M., et al. (2013), Rapid local acceleration of relativistic radiation-belt electrons by magnetospheric chorus, *Nature*, *504*, 411–414, doi:10.1038/nature12889.

Tu, W., R. Selesnick, X. Li, and M. Looper (2010), Quantification of the precipitation loss of radiation belt electrons observed by SAMPEX, *J. Geophys. Res.*, *115*, A07210, doi:10.1029/2009JA014949.

Turner, D. L., T. P. O'Brien, J. F. Fennell, S. G. Claudepierre, J. B. Blake, E. K. J. Kilpua, and H. Hietala (2015), The effects of geomagnetic storms on electrons in Earth's radiation belts, *Geophys. Res. Lett.*, *42*, 9176–9184, doi:10.1002/2015GL064747.

Ukhorskiy, A. Y., Y. Y. Shprits, B. J. Anderson, K. Takahashi, and R. M. Thorne (2010), Rapid scattering of radiation belt electrons by storm time EMIC waves, *Geophys. Res. Lett.*, *37*, L09101, doi:10.1029/2010GL042906.

Williams, D. J., G. Hernandez, and L. R. Lyons (1976), Simultaneous observations of the proton ring current and stable auroral red arcs, *J. Geophys. Res.*, *81*(4), 608–616, doi:10.1029/JA081i004p00608.

Woodger, L. A., A. J. Halford, R. M. Millan, M. P. McCarthy, D. M. Smith, G. S. Bowers, J. G. Sample, B. R. Anderson, and X. Liang (2015), A summary of the BARREL campaigns: Technique for studying electron precipitation, *J. Geophys. Res. Space Physics*, *120*, 4922–4935, doi:10.1002/2014JA020874.

Yahnin, A. G., T. A. Yahnina, N. V. Semenova, and B. B. Gvozdevsky (2014), Relativistic electron precipitation as seen by NOAA POES, in *Physics of Auroral Phenomena*, *Proc. XXXVII Annual Seminar (Apatity, Russia, 2014)*, pp. 46–50, Kola Science Center, Russian Academy of Sciences, Apatity, Murmansk, Russia.

Yando, K., R. M. Millan, J. C. Green, and D. S. Evans (2011), A Monte Carlo simulation of the NOAA POES Medium Energy Proton and Electron Detector instrument, *J. Geophys. Res.*, *116*, A10231, doi:10.1029/2011JA016671.

Zhao, H., X. Li, J. B. Blake, J. F. Fennell, S. G. Claudepierre, D. N. Baker, A. N. Jaynes, D. M. Malaspina, and S. G. Kanekal (2014), Peculiar pitch angle distribution of relativistic electrons in the inner radiation belt and slot region, *Geophys. Res. Lett.*, *41*, 2250–2257, doi:10.1002/2014GL059725.

Zhao, H., et al. (2015), The evolution of ring current ion energy density and energy content during geomagnetic storms based on Van Allen Probes measurements, *J. Geophys. Res. Space Physics*, *120*, 7493–7511, doi:10.1002/2015JA021533.

Zhao, H., et al. (2016), Ring current electron dynamics during geomagnetic storms based on the Van Allen Probes measurements, *J. Geophys. Res. Space Physics*, *121*, 3333–3346, doi:10.1002/2016JA022358.